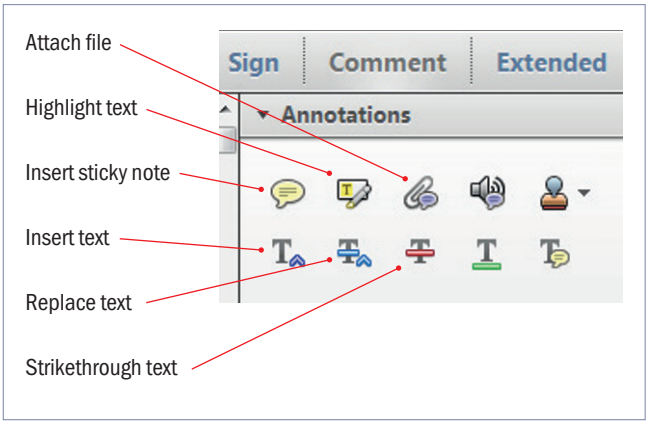
Making corrections to your proof

Please follow these instructions to mark changes or add notes to your proof. You can use Adobe Acrobat Reader (download the most recent version from **https://get.adobe.com**) or an open source PDF annotator.

For Adobe Reader, the tools you need to use are contained in **Annotations** in the **Comment** toolbar. You can also right-click on the text for several options. The most useful tools have been highlighted here. If you cannot make the desired change with the tools, please insert a sticky note describing the correction.

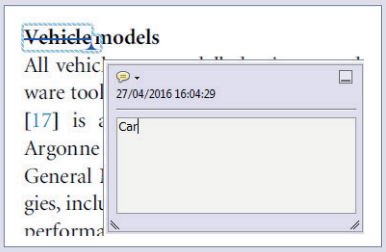
Please ensure all changes are visible via the 'Comments List' in the annotated PDF so that your corrections are not missed.



Do not attempt to directly edit the PDF file as changes will not be visible.

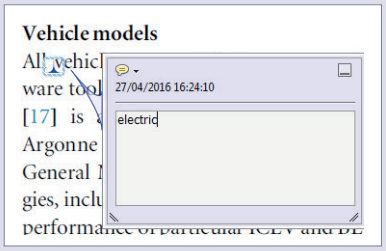
Replacing text

To replace text, highlight what you want to change then press the replace text icon, or right-click and press 'Add Note to Replace Text', then insert your text in the pop up box. Highlight the text and right click to style in bold, italic, superscript or subscript.



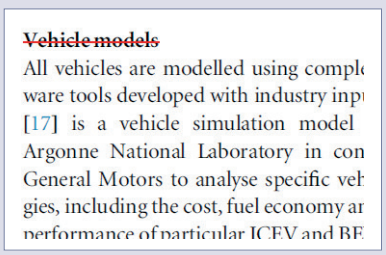
Inserting text

Place your cursor where you want to insert text, then press the insert text icon, or right-click and press 'Insert Text at Cursor', then insert your text in the pop up box. Highlight the text and right click to style in bold, italic, superscript or subscript.



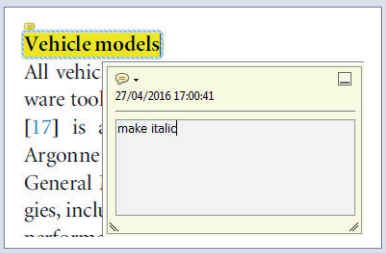
Deleting text

To delete text, highlight what you want to remove then press the strikethrough icon, or right-click and press 'Strikethrough Text'.



Highlighting text

To highlight text, with the cursor highlight the selected text then press the highlight text icon, or right-click and press 'Highlight text'. If you double click on this highlighted text you can add a comment.



QUERY FORM

JOURNAL: Journal of Physics D: Applied Physics

AUTHOR: R Jaiswar *et al*

TITLE: Nonlinear electrical transport in Fe_3O_4-decorated graphene nanoplatelets

ARTICLE ID: abc2f2

Your article has been processed in line with the journal style. Your changes will be reviewed by the Production Editor, and any amendments that do not comply with journal style or grammatical correctness will not be applied and will not appear in the published article.

The layout of this article has not yet been finalized. Therefore this proof may contain columns that are not fully balanced/matched or overlapping text in inline equations; these issues will be resolved once the final corrections have been incorporated.

Q1: Please check that the names of all authors as displayed in the proof are correct, and that all authors are linked to the correct affiliations. Please also confirm that the correct corresponding author has been indicated. Note that this is your last opportunity to review and amend this information before your article is published.

Q2: If an explicit acknowledgment of funding is required, please ensure that it is indicated in your article. If you already have an Acknowledgments section, please check that the information there is complete and correct.

Q3: Please check that the funding information below is correct for inclusion in the article metadata.
Fonds De La Recherche Scientifique - FNRS
Communauté française de Belgique

Q4: We have been provided with ORCID iDs for the authors as below. Please confirm whether the numbers are correct.
Sophie Hermans 0000-0003-4715-7964
Isabelle Huynen 0000-0002-8504-2896

Q5: Note that the supplementary data associated with your article will be hosted as supplied, and will not be processed by us. If you wish to supply new files, please send them along with your proof corrections.

Q6: Please be aware that the colour figures in this article will only appear in colour in the online version. If you require colour in the printed journal and have not previously arranged it, please contact the Production Editor now and refer to https://publishingsupport.iopscience.iop.org/questions/figures-journal-articles for pricing.

Q7: References were not cited sequentially. Hence, references have been renumbered from Ref.43. Please check.

Q8: Please check the edits made to the sentence ';The similar behavior...'.

Q9: Please check the details for any journal references that do not have a link as they may contain some incorrect information. If any journal references do not have a link, please update with correct details and supply a Crossref DOI if available.

Q10: Please provide the publisher location details for references [11, 23, 48, 60].

Q11: Please check whether reference 58 is possibly duplicate of reference 54?

UNCORRECTED PROOF

IOP Publishing Journal of Physics D: Applied Physics
J. Phys. D: Appl. Phys. **0** (2020) xxxxxx (11pp) https://doi.org/10.1088/1361-6463/abc2f2

Nonlinear electrical transport in Fe_3O_4-decorated graphene nanoplatelets

Rajkumar Jaiswar[1], Francisco Mederos-Henry[2], Sophie Hermans[2], Jean-Pierre Raskin[1] and Isabelle Huynen[1]

[1] Institute of Information and Communication Technologies, Electronics and Applied Mathematics (ICTEAM), ELEN Division, Université catholique de Louvain, 3 place du Levant, 1348 Louvain-la-Neuve, Belgium
[2] Institute of Condensed Matter and Nanosciences (IMCN), Division of Molecular Chemistry, Materials and Catalysis (MOST), Place Louis Pasteur 1, Université catholique de Louvain, 1348 Louvain-la-Neuve, Belgium

E-mail: isabelle.huynen@uclouvain.be

Received 27 July 2020, revised 8 October 2020
Accepted for publication 20 October 2020
Published xx xx xxxx

Abstract

This paper investigates the nonlinear properties of graphene nanoplatelets (GNPs), decorated with Fe_3O_4 magnetic nanoparticles (MaNPs). Nanocomposite MaNP/GNP samples were prepared by a solvothermal method with three different MaNP loading concentrations of 17 wt%, 28 wt% and 40 wt%, and deposited on a metallic interdigitated electrode (IDE). Three different models are proposed to assess measurements, with the objective to explain the electronic transport in the nanocomposites. At first, a thermionic transport model is proposed to fit the DC nonlinear current–voltage characteristics for the three concentrations. It is observed that the barrier height decreases to 0.312, 0.310 and 0.281 eV, following a decrease in the MaNP loading. A second model, dynamic random resistor network (DRRN) further shows that the impedance of IDE increases following the decreasing MaNP loading rate, 40 wt% > 28 wt% > 17 wt%, and that charge transport takes place through a resistor–capacitor (RC) rectifying percolating network. Finally, impedance spectroscopy performed at different applied DC biases shows that a constant phase element (CPE) is necessary in the equivalent circuit in order to fit the Cole–Cole plot AC response of the IDE, instead of the classical parallel RC circuit. The presence of the CPE confirms the hypothesis of random phenomena occurring in the transport according to the DRRN model. CPE is associated with a spatial distribution of different RC circuits, due to disorderness that arises from inhomogeneities in the Fe_3O_4–GNP samples.

Supplementary material for this article is available online

Keywords: nanostructure, magnetite, impedance spectroscopy, equivalent circuit, graphene

(Some figures may appear in colour only in the online journal)

1. Introduction

This paper explores the potential of graphene nanoplatelets (GNPs), which provide a large 2D surface area for functionalization by nanoparticles (NPs) for a wide variety of applications. In [1], Mederos-Henry *et al* reported different techniques to decorate graphene oxide (GO) with magnetite nanoparticles (MaNPs). GO is intrinsically a bad conductor or highly resistive carbon material, due to the presence of defects and oxygenated groups (such as –COOH, –OH, –COC, depending on the technique used to oxidize graphite), and cannot be utilized directly for electromagnetic interference (EMI)

 © 2020 IOP Publishing Ltd Printed in the UK

shielding applications requiring conductive materials. Thus, unmodified GNPs and their combination with various doping compounds (such as Fe_3O_4, nickel, cobalt) become the natural alternative for EMI-related applications [2].

In general, exfoliated GNPs with high surface area (approx. 900 m^2 $g-^1$) are ideal for physical and chemical functionalization. They can be used in composite structures in combination with a variety of inorganic materials such as metals or metal oxides [3, 4]. In the past, the growing interest of the scientific community for coupling nano-carbons and magnetic materials has led to the production of multifunctional structures such as variable EMI shielding structures with different loading rates (LRs) [5], improved Li-ion capacitors [6], sensors and detectors [7, 8], magnetic switches [9] and solar cells [10]. Transition metal or metal oxide NPs such as Fe, Co, Ni, Fe_3O_4, Fe_2O_3 and Co_3O_4 [11–13] anchored on graphene nanosheets, have been extensively reported due to their exceptional electrical and magnetic properties derived from synergetic effects such as rectifying behavior, enhanced magnetic saturation, magneto-resistance, or tunable electromagnetic parameters [14–18].

The charge transport phenomenon through the hybrid composite depends on a number of factors such as chemical functionalization, interfacial interactions, temperature, chemical treatments, etc [19, 20]. For carbon nanotubes (CNTs) decorated with iron oxide, a few scientific reports presented the DC characterization of electronic properties and charge transfer mechanisms through the hybrid composite [21]. Also, some studies investigated the current behavior under the variation of temperature, magnetic field and applied bias, in order to explore the electronic properties of these nanostructured materials [21, 22]. There are many reports about the synthesis of Fe_3O_4@GNP nanocomposites, mainly focusing on their use for energy storage or sensor applications [23, 24]. Also, successful theoretical approaches to the formation/stability of graphene-like systems that are interacting/decorated with different metal-atom-containing species are available, and which also make use of the temperature molecular dynamics and *ab initio* molecular dynamics tools [25–28]. Nonetheless, a thorough analysis of the charge transport behavior and electronic properties of these nanocomposites has not yet been realized. Hence, in this paper, we explore the electronic properties and current transport mechanism of Fe_3O_4@GNP nanocomposites having different LRs of Fe_3O_4 NPs on GNPs, clearly demonstrating the impact of the MaNPs on the electrical properties of the graphenic material.

2. Materials and methods

GNPs decorated with different Fe_3O_4NP LRs were synthesized using a solvothermal method, as described in section 2.1. The resulting materials were then characterized by x-ray powder diffraction (XRPD), thermogravimetric analysis (TGA) and transmission electron microscopy (TEM) to determine the deposited NPs' chemical composition, size, LR and spatial distribution.

2.1. Synthesis of MaNPs@GNPs

GNPs were supplied by TIMCAL (Switzerland), $FeCl_3$•$6H_2O$, polyethylene glycol PEG-400, ethylene glycol (EG) and NaOH pellets were purchased from Sigma Aldrich, Merck, Alfa Aesar or VWR and used as received.

The solvothermal production of GNPs decorated with magnetite NPs has been carried out as described for GO in [1]. In a typical synthesis, 250 mg of GNPs were dispersed into a mixture composed of 67 ml EG, 33 ml polyethylene glycol 400 (PEG-400) and 33 ml Milli-Q water. The suspension was sonicated for 2 h in a VWR ultrasound cleaner USC 1200-THD at 80 W sonication power. Afterwards, a certain amount of $FeCl_3$•$6H_2O$ was added under magnetic stirring in order to obtain the desired Fe_3O_4/GNP (% w/w) LR (e.g. 484 mg for an intended 40% LR). After complete dissolution of the salt, crushed NaOH pellets were added until the solution pH value was set at 13. The mixture was then transferred into a stainless-steel autoclave, heated to 180 °C (approx. 50 min) and maintained at that temperature for 23 h. The autoclave temperature was automatically regulated by a Parr 4836 temperature controller (Parr Instrument Company, USA) having an average heating rate of 4 °C min^{-1}. The autoclave inner atmosphere was neither purged nor modified in any manner during the synthesis, while the system pressure was left to build up during heating without any type of external control. When the heating time was completed, the autoclave was immediately immersed in an ice bath and cooled to ambient temperature. The obtained products were separated by magnetic decantation, filtered over a PVDF filter (Millipore GVWP02500, 0.22 μm pore size) and rinsed six times, alternating Milli-Q water and ethanol. Afterwards, they were dried under vacuum at room temperature for 12 h.

2.2. Scanning and transmission electron microscopies (SEM and TEM)

Samples were dispersed in hexane by sonication. Three drops of the supernatant were then deposited onto a holey carbon film supported on a copper grid (C-flat, Protochips, USA) and left to dry overnight at room temperature under vacuum. The as-prepared grids were then analyzed by SEM and TEM, as described below.

A FEG-SEM Ultra55 instrument (Carl Zeiss, Germany) equipped with an Oxford Inca EDX system (Oxford Instruments, UK) was used. Images were acquired with Smart SEM software (Carl Zeiss, Germany) at different acceleration voltages ranging between 3–15 keV, using InLens and SE2 detectors.

TEM images were obtained on an LEO 922 Omega Energy Filter TEM operating at 120 kV.

2.3. Electrical DC and AC measurements

DC current–voltage curves were measured using an Agilent source meter connected to interdigitated electrodes (IDEs), as described in section 2.4. Low-frequency bias-dependent measurement was performed using a VNA ENA5061B connected

through Bias-Tee to a source meter. Scattering parameters and current–voltage characteristics were obtained under applied voltage bias. The IDEs were calibrated using the SOLT method [29] to measure the scattering parameters for each sample [30]. This paper focuses on the electrical properties of the nanocomposites at low frequencies under DC applied bias. The analysis of the behavior under DC magnetic field could also be relevant, but is not addressed here.

2.4. Sample preparation

The Fe_3O_4@GNP composites having 17 wt%, 28 wt% and 40 wt% MaNP LRs were suspended in ethanol (1:1 wt vol^{-1} ratio). A homogeneous dark suspension was obtained after 1 min of sonication. A similar procedure was also followed to prepare a pure GNP suspension [1]. As shown in figure 1, the suspension was then deposited by drop-casting between copper IDEs fabricated on a Rogers 3000 substrate having permittivity of $\varepsilon_r = 3.3$. The casted film was dried under ambient atmosphere for 2 h and the electrodes were carefully cleaned with ethanol. The IDE illustrated in figure 1 was chosen due to its ease of fabrication and simplicity in modeling. Its theoretical calculation can be found in [26]. IDE structures are widely used in sensing applications due to their excellent ability to detect the smallest change in the properties of the materials under test [31–33].

3. Results and discussion

3.1. Fe_3O_4@GNP characterization

XRPD and TGA characterization results are given in the Supplementary Information (SI) (available online at https://stacks.iop.org/JPD/00/0000/mmedia). The former technique confirmed that the deposited NPs are, in all cases, mainly composed of magnetite, while the latter informed us of the achieved MaNP LRs. Figure 2 shows a series of SEM and TEM images of the Fe_3O_4@GNP nanocomposites produced with different MaNP LRs. It can be seen that the solvothermal strategy produced nanocomposites in which the GNPs are densely decorated with MaNPs. In all decorated materials, the spatial distribution of the deposited Fe_3O_4 NPs is mostly homogeneous even though small areas of the nanoplatelets were left uncovered. This might be due to the highly reduced state of the used GNPs. Indeed, it has been shown that NPs distribute more homogeneously on nanocarbon supports possessing a higher rate of oxygenated surface functions that act as nucleation centers [1].

3.2. DC properties

Figure 3(a) presents the nonlinear current–voltage behavior of the Fe_3O_4@GNP composites for 17 wt%, 28 wt% and 40 wt% LRs. The dI/dV versus V parabolic conductance curves in figure 3(b) suggest that the electron transport is dominated by a tunneling mechanism between conductive percolative paths

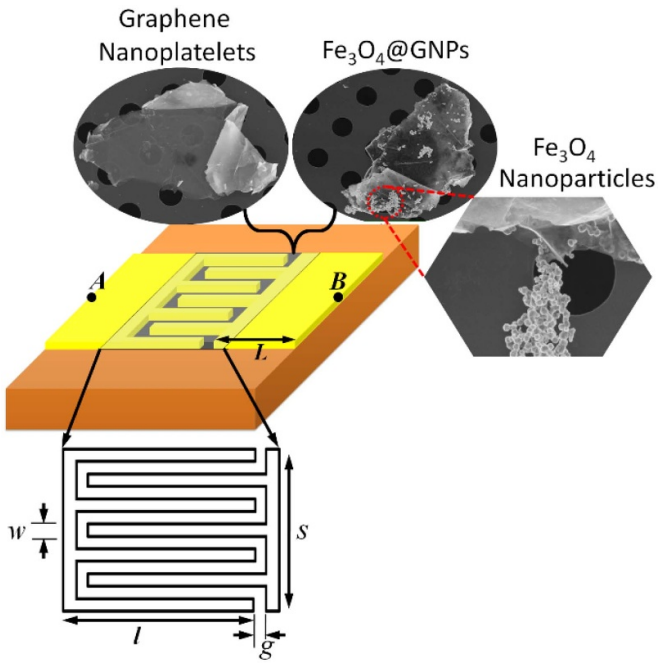


Figure 1. (top) TEM images of GNPs and Fe_3O_4. (bottom) Schematic of IDEs having finger dimensions of: w = 0.4, g = 0.2, s = 4, l = 17.1, L = 16.5. Units in mm.

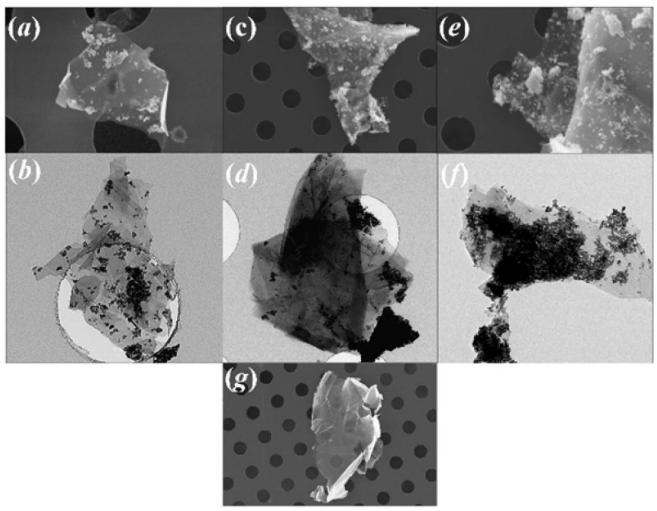


Figure 2. SEM (top) and TEM (bottom) images of Fe_3O_4@GNPs with an LR of magnetite (Fe_3O_4) NPs: (a) and (b) 17 wt%, (c) and (d) 28 wt%, (e) and (f) 40 wt% (g) SEM micrograph of pristine GNPs.

[21, 22, 34]. In a general scenario, pure Fe_3O_4@GNPs distributed homogeneously throughout the powder forming a random resistor–capacitor-like network.

The electronic properties of bulk Fe_3O_4 are quite different to that of any other transition metal oxide. Magnetite crystallizes with an inverse spinel cubic structure at room temperature and possesses a weak electrical conductivity of $\sigma \approx 50$ S cm^{-1} [35]. In the octahedral coordination spheres in the crystal structure, Fe^{3+} and $Fe^{2+}(Fe_{oct})$ ions are ferromagnetically coupled through a so-called double-exchange

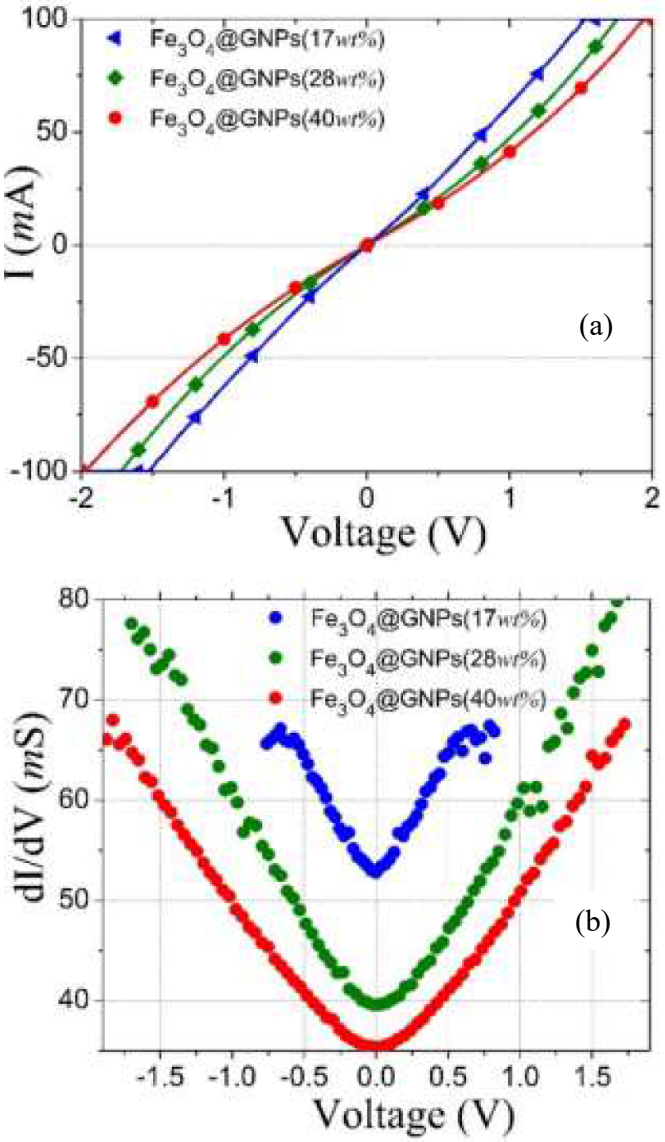


Figure 3. (a) Current–voltage characteristics according to (1) for 17 wt%, 28 wt% and 40 wt% samples and (b) d*I*/d*V*-*V* conductance curves according to (2).

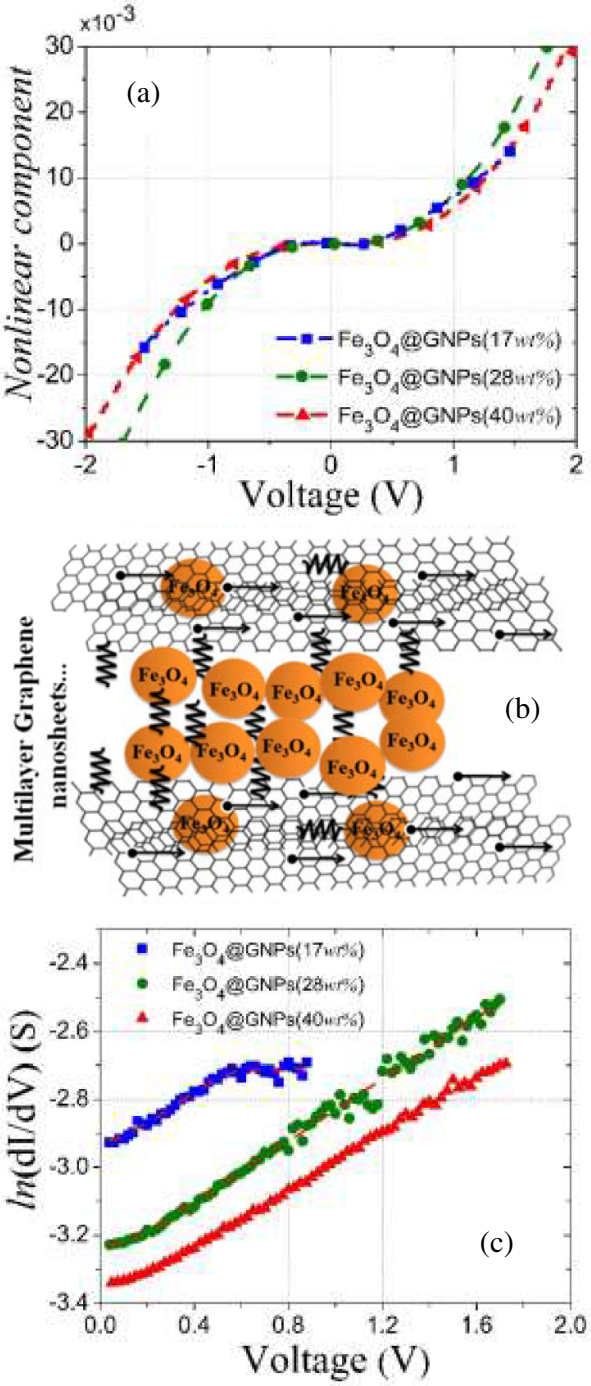


Figure 4. (a) Nonlinear component extracted from original current curves, for the composite samples 17 wt%, 28 wt% and 40 wt%. (b) Schematic illustration of charge transport indicated by arrows inside the Fe_3O_4@GNP nanocomposite: electronic transport occurs in the graphene sheets and through Fe_3O_4 via tunneling. (c) $\ln(\mathrm{d}I/\mathrm{d}V)$ *versus* V from (2).

mechanism, which dominates the electronic properties of magnetite. Electron hopping between the Fe^{2+} and Fe^{3+} sites of the octahedral holes mediates the relatively moderate room-temperature conductivity of magnetite [36, 37].

Multilayer graphitic sheets have limited defects in 2D-sp^2 hybridized carbon planes, but Fe_3O_4 entities attached to the graphene surface disrupt the extended sp^2 conjugated network of nanosheets, inducing a significant decrease in conductivity [38]. The electron conduction in the percolating system occurs mainly through the interconnected network in the hybrid composite, which is illustrated in figure 4(b).

The conductivity is thus governed by the nano-inclusions and contacts between them. These observations suggest that GNPs homogeneously decorated with Fe_3O_4 NPs form a distributed resistor–capacitor-like network spread randomly. This might be the reason for the symmetrically nonlinear electrical behavior of the hybrid system.

3.2.1. Thermionic model. As shown in figure 3, the *I*–*V* curve of Fe_3O_4@GNPs and conductance curves d*I*/d*V* versus *V* display a loading-dependent behavior.

Table 1. Parameters of the thermionic equation (1).

Compounds	Φ (eV)	n	$\mathbf{I_s}$(mA)
40 wt%	0.3116	96	84
28 wt%	0.3104	90	88
17 wt%	0.2808	193	279

As the magnetite LR increases, the total conductance $(dI/dV)_{V=0}$ decreases with increasing LR, following 17 wt% < 28 wt% < 40 wt%. The electron transport in the composite system takes place through circuit elements between GNP-Fe_3O_4-GNP nanostructures as well as through clusters of stacked nanosheets of GNPs–GNPs as visible in the SEM/TEM images (figure 2). As the LR of magnetite increases, the resistive-capacitive nature of the composite increases too. This results in a more nonlinear charge transfer through the disordered structures, represented by a distribution of energy barriers and tunneling processes between the nearest neighbors. In the thermionic charge transport model, the current dependence on the applied bias is expressed as [39]:

$$I = I_s\left(e^{qV/nkT} - 1\right), \tag{1}$$

where $I_s = A_e A^{**} T^2 e^{(-q\varphi/kT)}$ is the dark saturation current, A_e is the active area of the contact electrode, A^{**} is the Richardson constant, k is the Boltzmann constant, T is the temperature, φ is the effective barrier height and n is the number of junctions along the percolation network [35]. Taking the derivative, $(dI/dV = (dI_{i+1} - dI_i)/(dV_{i+1} - dV_i)$ where i is the number of data points in the plot of equation (1), and plotting its logarithm versus applied bias, the result can be fitted with a linear equation as follows:

$$\ln(dI/dV) = \ln(I_s q/nkT) + qV/nkT. \tag{2}$$

In expression (2), the ideality factor n can be calculated from the slope of the line, and its zero-intercept the saturation current I_s and the effective barrier height φ can be extracted, as given in table 1 [40].

From table 1, it is observed that the barrier height increases with loading concentration whereas the dark saturation current is reduced. Sample 17 wt% has the highest saturation current at 279 mA, which may be large enough for charge carriers to cross over any barrier without difficulty. This is also observed in the *I–V* curve figure(3)(a) which shows overall near-linear ohmic current behavior. The other two samples, 40 wt% and 28 wt%, have comparatively high barrier height (φ), i.e. 0.3116 and 0.3104 eV, and much lower saturation current I_s,84 and 88 mA, respectively, meaning a more diode-like rectifying behavior visible in the *I–V* curve. A heterostructure material consists of two or more materials having different electronic properties where junction interfaces have different Fermi-level energies causing a barrier for charge transport. In our nanocomposite, the material properties are characterized by the work function (φ) difference between Fe_3O_4 and GNPs, which is $\varphi_{magnetite} - \varphi_{GNPs} \approx 0.65$ eV. Hence, under external bias, the field-assisted electron tunneling through insulating channels is thereby changing the conductivity and nonlinear conduction of individual junctions [22].

Figure 4(a) shows the nonlinear component of the current for the whole composite obtained by subtracting the linear values from the N-degree polynomial fitting of the current.Figure 4(b) shows a schematic diagram illustrating the microscopic arrangements of Fe_3O_4 and GNPs responsible for multiple reflections, scattering and interfacial polarization mechanisms mimicking the lossy mechanisms in the composites. Figure 4(c) represents the logarithmic curve $\ln(dI/dV)$ *versus* V curve from equation (2). It has to be mentioned that the measurement of IDC empty or covered with pristine GNPs showed no nonlinear behavior.

The thermionic transport model allows us to fit current curves, but is unable to provide information about the link between disordered media and its conduction behavior. In order to further investigate the conduction through disordered media such as in the Fe_3O_4@graphene nanocomposite, another model is described in section 3.2.2. It assumes that the percolating network is well above the critical value of percolation even at low voltage; hence, a significant conductance is obtained, as can be seen in figure 3(b).

3.2.2. Dynamic random nonlinear network. Magnetite crystals possess bad conducting properties and, when distributed in a conductive matrix, can be modeled as a nonlinear random resistor network in which conducting/insulating inclusions consist of microscopic circuit elements. The dynamic-random resistor-network (DRRN) model assumes that conduction is linear, but for a sufficiently strong local field, a non-conducting channel becomes conducting on the microscopic scale caused by nonlinear hopping or tunneling of charge carriers [40, 41]. Gefen *et al* found that the DRRN model fitted very well experimental *I–V* curves, using the equation $I = GV + G'V^b$ where G is linear conductance and G' is higher order conductance, which suggests that current transport takes place preferably through tunneling [40, 41]. However, Gupta *et al* [42] suggested that exponential terms describe better the entire nonlinear regime of current–voltage curves rather than the power-law behavior of a polynomial function. Furthermore, it has been suggested that quantum-mechanical tunneling between the conductive phases takes place across the potential barriers and its conductance falls off exponentially with the tunneling distance, so that the current is a nonlinear function of the potential difference across the macroscopic bonds [42, 43]. Therefore, the conductance curve can be fitted to the following equation, which results from homogenization over various conductances associated with different percolative channels through the Fe_3O_4@GNP composite [42]:

$$G = G_0 + G_d[1 - \exp(-\lambda\Delta V)^n], \tag{3}$$

where:

- G is obtained as $G = (dI/dV) = (dI_{i+1} - dI_i)/(dV_{i+1} - dV_i)$, where i is the number of data points. $\Delta V = V - V_g, G_d =$

Table 2. Fitted values for the exponential equation (3).

Compounds	G_o	G_f	n	λ
17%	0.053	0.100	1.016	0.50
28%	0.040	0.093	1.75	0.47
40%	0.035	0.085	1.85	0.38

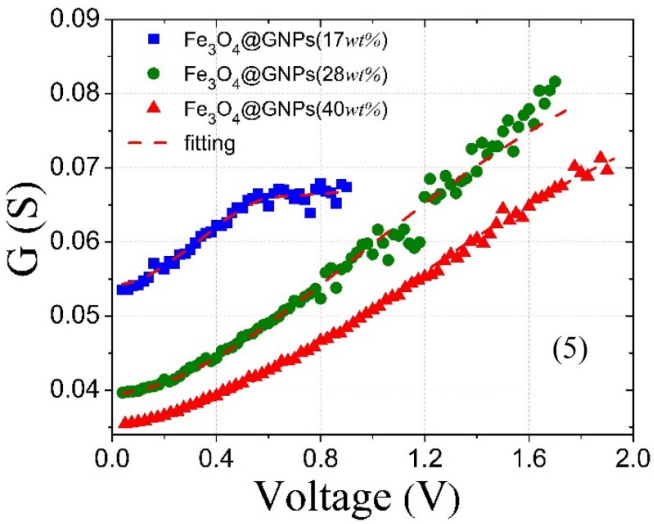


Figure 5. Conductance versus positive applied bias for the three samples fitted with equation (3).

$G_f - G_0$, V_g is a certain constant voltage up to which conductance is nonzero, in our case $V_g = 0$

- G_f is saturation conductance at higher bias while λ and n are the coefficient and exponent of nonlinearity, respectively.
- The intercept G_0 can be given as [44, 45]:

$$G_0 = (dI/dV)_{V=0} \propto \exp\left[-\sqrt{\frac{8\chi d\mathrm{E}_c}{k_B T}}\right], \qquad (4)$$

where $\chi = \sqrt{2m\phi/\hbar^2}$ and φ, d and E_c are the barrier height, tunneling distance and electrostatic activation energy, respectively. The extracted fitting parameters of equation (3) calculated from $G = (dI/dV)$ are given in table 2 and plotted in figure 5.

The conductive behavior of each microscopic circuit element is intrinsically nonlinear, and this nonlinearity is amplified due to the complex structure of the distributed conducting network traversing the entire hybrid system. By applying equation (3), we observed from table 2 that the exponent of nonlinearity, n, increases from sample 17 wt% to 40 wt% and the corresponding conductance G_f and G_0 is higher for 17 wt% than for 28 wt% and 40 wt%. This may be attributed to a lower number of available direct conductive pathways for the charge transport when increasing the magnetite LR, as expected from what has been described above. Under AC regime, the nonlinear current produces frequency-independent behavior of resistances at different biases applied over a wide low-frequency range, as will be discussed below.

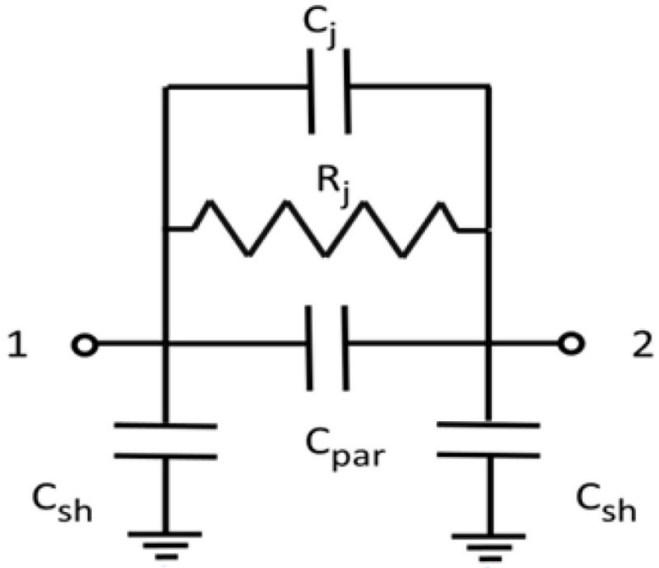


Figure 6. Equivalent circuit of impedance Z embedded in capacitances C_{sh} and C_{par} of an empty IDE.

3.3. AC properties

3.3.1. Impedance measurements. AC transmission behavior has been measured, for all three materials deposited between the IDE, at different applied voltages and between 40 kHz–3 GHz. In the past, Ouriemi *et al* [41] reported on the DC and AC response of unmodified semiconducting CNTs in between IDEs, and proposed an equivalent circuit involving elements accounting for the nonlinear electrical characteristics of semiconducting CNTs. A similar approach is discussed here for the Fe_3O_4@GNP nanocomposites. The impedance Z between the input and output port of the IDE is extracted from the equivalent circuit shown in figure 6, while figures 7 and 8 show the measured impedance Z for the three Fe_3O_4@GNP samples 40 wt%, 28 wt% and 17 wt% as well as for pristine GNPs. Z is extracted from admittance matrix Y obtained by S to Y conversion formulas [46] and the corresponding π-circuit model shown in figure 6. The admittance matrix Y is written as [47]:

$$\begin{aligned} Y &= \begin{bmatrix} Y_{11} & Y_{12} \\ Y_{21} & Y_{22} \end{bmatrix} \\ &= \frac{1}{R_j(V)} \begin{bmatrix} 1 & -1 \\ -1 & 1 \end{bmatrix} \\ &\quad + j\omega \begin{bmatrix} C_{sh1} + C_j(V) + C_{par} & -C_j(V) + C_{par} \\ C_j(V) + C_{par} & C_{sh2} + C_j(V) + C_{par} \end{bmatrix} \end{aligned}, \qquad (5)$$

where $R_j(V), C_j(V)$ are voltage-dependent junction resistance and capacitance of a material whereas C_{sh}, C_{par} are shunt pad-capacitances and parasitic capacitance ($C_{par} = C_{pp} + C_{fp}$), and C_{pp}, C_{fp} are pad-to-pad and finger-to-pad capacitance in an empty line, respectively. When the sample materials are deposited between the IDE, C_{par} is assumed to be negligible (for the sake of simplicity) since the structure

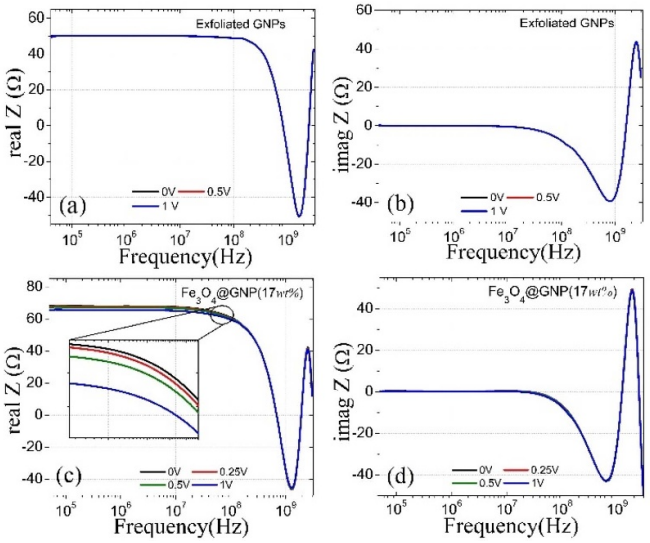


Figure 7. Measured real and imaginary part of Z impedance for (a) and (b) GNP sample (c) and (d) 17 wt% sample. Black: 0 V, red: 0.25 V, green: 0.75 V, blue: 1 V.

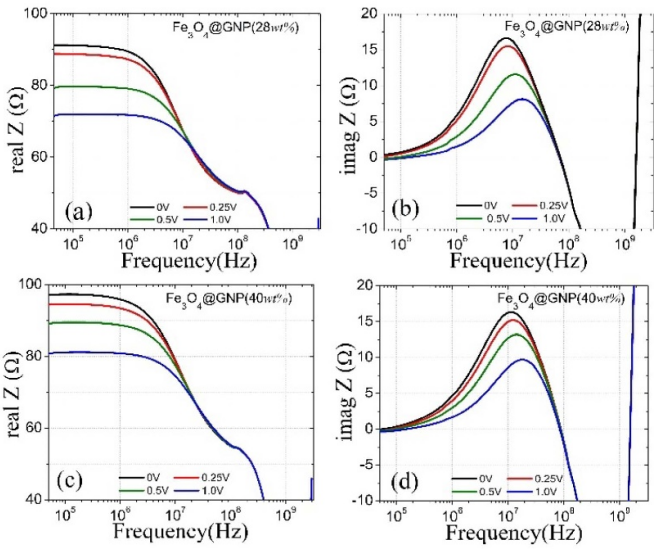


Figure 8. Measured real and imaginary part of Z impedance (a) and (b) 28 wt% sample (c) and (d) 40 wt% sample. Black: 0 V, red: 0.25 V, green: 0.75 V, blue: 1 V.

behaves more like a resistive line. Hence, voltage-dependent resistance and capacitance associated with series impedance $Z = R_{\rm tot} + 1/j\omega\, C_{\rm tot}$ are easily represented from the Y_{21} parameter as [48]:

$$C_{tot} = \frac{Im\,(Y_{21}\,(V))}{\omega} = C_{jo}\left(1 - \frac{V}{\varphi_{bi}}\right)^{-M} + C_{par},$$

$$R_{tot} = \frac{1}{Re\,(Y_{21}\,(V))} = R_j\,(V) + R_s, \qquad (6)$$

where C_{j0} and R_s are the junction capacitance and resistance at zero bias, whereas V, φ_{bi} are the applied bias and built-in potential and M represents the doping profile of the junction layer. This circuit can be put in correlation with figure 4(b), since nonlinear resistance and capacitance model the interaction at the interface between GNP and Fe_3O_4 NPs, while $C_{\rm sh}$ and $C_{\rm p}$ are associated with the IDE geometry in figure 1.

Figures 7(a) and (b) show that the IDE covered with unmodified GNPs has a resistance real(Z) of 50 Ω between 50 kHz–100 MHz and does not vary with applied bias voltage since unmodified GNP is a purely conductive material. Sample 17 wt% having the lowest MaNP loading amongst all has a resistance real(Z) around 67–69 Ω and almost negligible variation is observed with applied bias. Likewise, its imaginary part Im(Z) remains zero in the low-frequency spectrum, as shown in figures 7(c) and (d).

The significant variation in impedance is observed for samples 40 wt% and 28 wt%. It is well known that increasing the applied bias injects more charge carriers, hence increasing the conductance of the sample, which is very well observed here. In figures 8(a) and (c), samples 28 wt% and 40 wt% have resistance real(Z) around 91 and 98 Ω at zero bias while it decreases to 72 and 81 Ω at applied DC voltage of 1 V, respectively, between 50 kHz–100 MHz. The reactance part of these samples imag(Z) also shows a significant peak shift as well as a decrease in magnitude between 10–100 MHz, as shown in figures 8(b) and (d). The reactances have their maximum value at different frequencies (f_o), called relaxation frequencies, which depend on increasing applied bias. Generally, a frequency f_0 is a threshold level up to which sample conductivity is frequency independent at low frequencies. Therefore, a higher f_0 indicates better connectivity between the particles and a smaller correlation length [49, 50]. This concept describes the mechanism of current flow in which electrons cross over the potential barrier with finite exponential behavior where large isolated clusters as well as the main backbone percolating network contribute to the conduction process. The correlation length is the length-scale between two points in a finite cluster or junctions through which charge transport takes place in a disordered system. Higher threshold frequency f_o is thus indicative of smaller correlation lengths, which gives rise to better conductivity and less disorder in the system [51]. The peak observed above 1 GHz is attributed to the intrinsic resonance of the IDE and is therefore insensitive to DC bias. Figures 7 and 8 also show that the real part of Z clearly increases from 70 Ω for 17% Fe_3O_4 loading to 90 Ω for 40%. This is due to the increase of the magnetic permeability of the medium surrounding the IDE, due to the magnetic nature of the MaNPs, which induces an increase of the impedance of the IDE through its characteristic impedance proportional to permeability [52].

3.3.2. Impedance spectroscopy model. To investigate further the transport phenomenon in our samples, we present our results using the Cole–Cole representation. Figure 9 represents the measured curve Im(Z) versus Real(Z) for both samples 40 wt% and 28 wt% under applied bias. Sample 17 wt% does not show any significant variation in the impedance under applied bias, as can be seen in figures 7(a) and (b).

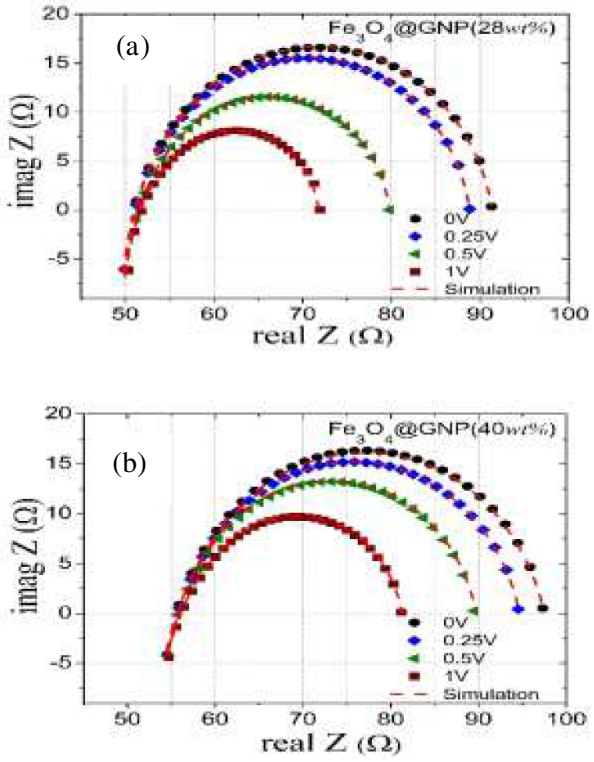


Figure 9. Cole–Cole plots for Fe_3O_4@GNP composites under applied bias (0–1 V) for the (a) 28 wt% sample and (b) 40 wt% sample. Dashed lines show Cole–Cole fit.

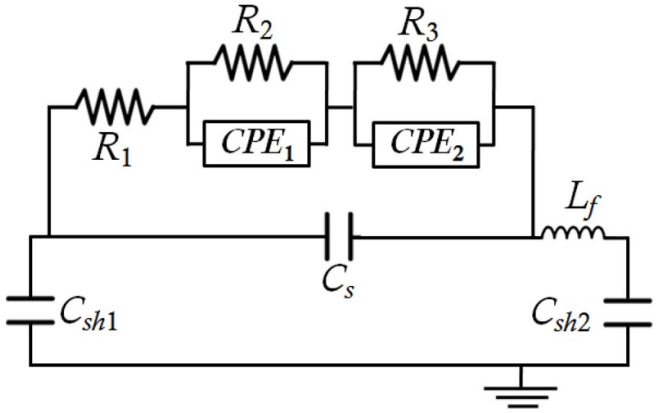


Figure 10. Equivalent circuit model for Fe_3O_4@GNP composites including IDEs TL.

Table 3. Extracted equivalent circuit element values for sample 40 wt%.

V	R_1	R_2	R_3	CPE_1		CPE_2	
				Q_1	α_1	Q_2	α_2
0	50.36	36.18	10.96	4.3013e-09	0.86055	2.9266e-08	0.77150
0.25	50.35	33.80	10.51	3.9513e-09	0.87131	2.0927e-08	0.78615
0.5	50.35	29.20	10.17	3.4706e-09	0.87925	1.1315e-08	0.81636
1.0	50.35	19.41	11.51	3.0539e-09	0.89714	0.5912e-08	0.83918

Figure 9 reveals that curves are flattened/squeezed compared with perfect hemi-circles that are associated with impedance spectroscopy theory to simple RC parallel circuits.

As explained in [53, 54], the deformation of the curves with respect to RC behavior is associated with a spatial distribution of RC circuits having different time constants. These distributed circuits mimic the dispersive and disordered nature of the dielectric or carbon-based material, along with spatial inhomogeneity, doping concentration and frequency dependence of the conductivity of the nanocomposite powders. Measured complex impedance data can be used to construct the equivalent circuit of figure 10, which helps to represent the charge transport mechanism [53, 55]. This corresponds to the Z impedance of the IDE covered by Fe_3O_4@GNP NPs.

The data summarized for circuit elements in tables 3 and 4 for samples 40 wt% and 28 wt%, respectively, show values under applied bias from 0–1 V. The Cole–Cole plots comprising squeezed semicircles are fitted with the equivalent circuit shown in figure 10, which consists of a serial combination of a two parallel connection of resistances and constant phase elements (CPE) as $[R_2||CPE_1]$ and d $[R_3||CPE_2]$, the whole connected in series with resistance R_1. The two $R-CPE$ blocks in the circuit represent the presence of different electrical characteristics in the material: Fe_3O_4 contribution is represented by $[R_2||CPE_1]$, while the bulk property of the carbon material is represented by $[R_3||CPE_2]$. Interactions between CPE blocks are illustrated in figure 4(b). The resistive contribution R_2 is higher than R_3 due to the insulating nature of the Fe_3O_4 oxide, while GNPs are more conductive. The presence of the metallic IDE itself is represented by $R_{1,}$ accounting for ohmic resistance of the IDE, while C_s is its interdigitated capacitance and L_s its inductance [56, 57].

CPE models distributed circuit elements associated with the dispersive and disordered nature of the Fe_3O_4 and GNP materials supporting the electronic transport in the structure schematized in figure 4(b). CPE takes into account the distributed energy barriers and time constants caused by the inhomogeneous distribution of resistivity and/or dielectric constant and provides the excellent fitting to the measured impedance of disordered materials [46, 58]. CPE has impedance in the form of:

$$Z_Q(\omega) = (j\omega)^{-\alpha} Q^{-1}, \tag{7}$$

where Q is a physical material parameter independent of frequency and α is the exponent having the value $0 < \alpha < 1$. The exponent α describes the degree of capacitive nature, i.e. $\alpha = 1$ represents capacitive behavior, and $\alpha < 1$ is a discontinuous element [56].

R_e Now, total impedance $Z_{CPE-Total}$ of the $R-CPE$ circuit of figure 10 having additional parallel resistances R_2 and R_3 can be written as [57]:

$$Z_{CPEi} = (j\omega)^{-\alpha_i} Q_i^{-1},$$

$$Z_{CPE\,Total} = \frac{Z_{CPE1} R_2}{Z_{CPE1} + R_2} + \frac{Z_{CPE2} R_3}{Z_{CPE2} + R_3}. \tag{8}$$

The total impedance is fitted with the measured impedance shown in figure 9, using parameter α_1 and Q_1 for CPE_1 and α_2

Table 4. Extracted equivalent circuit element values for sample 28 wt%.

V	R_1	R_2	R_3	CPE_1		CPE_2	
				Q_1	α_1	Q_2	α_2
0	50.36	36.18	10.96	4.3013e-09	0.86055	2.9266e-08	0.77150
0.25	50.35	33.80	10.51	3.9513e-09	0.87131	2.0927e-08	0.78615
0.5	50.35	29.20	10.17	3.4706e-09	0.87925	1.1315e-08	0.81636
1.0	50.35	19.41	11.51	3.0539e-09	0.89714	0.5912e-08	0.83918

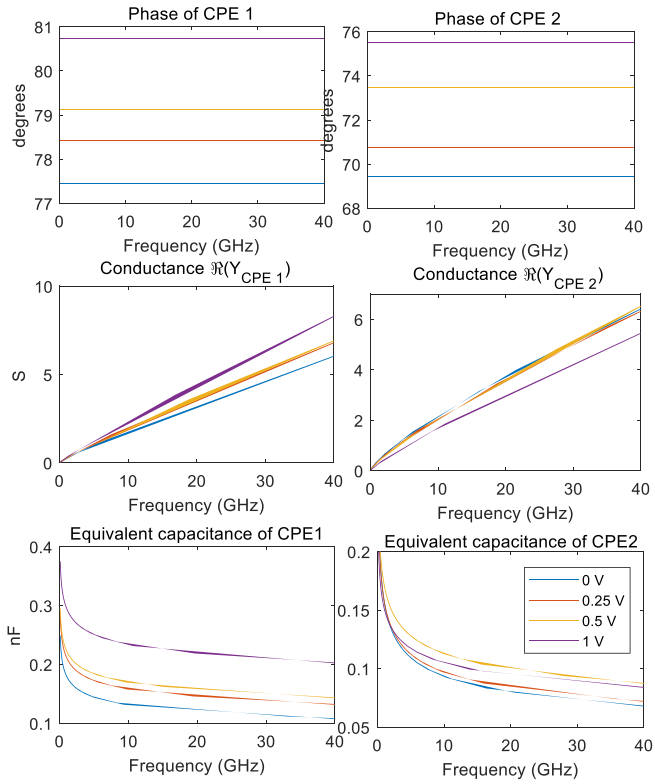


Figure 11. Frequency behavior of CPE elements for the 28 wt% sample.

and Q_2 for CPE_2, as defined in figure 10. It is observed from tables 3 and 4 that under increasing applied voltage, as more and more charge carriers are injected, the impedance of the deposited material is reduced, since α_i increases. For samples 40 wt% and 28 wt%, under applied bias, the decrease of the resistances and *CPEs* indicates smaller correlation lengths, which correspond to an increase in conductivity along with a shift in critical onset frequency f_0 observed in figure 8. As observed in figure 5, there is minimal difference in the DC behavior of the samples, particularly 40 wt% and 28 wt% composites. DC flow is less sensitive than AC flow, which means the frequency-dependent AC properties are more sensitive to the morphology of the nanocomposite than DC properties. The critical frequency f_0 and characteristic length are greatly influenced by the LR of magnetic NPs on GNPs, but there may be other factors influencing current transport such as energetic disorder in the system and interfacial scattering. Overall, it may be inferred that disorderness or the spatial distribution of inclusions can play an important role in charge transport phenomena in this type of nanocomposite [59, 60].

Figure 11 illustrates the impact of the above factors on the frequency dependence of CPE elements for the 28 wt% sample, derived from parameters in table 3. As expected, the phase of the two CPEs is constant versus frequency. However, the real part of each admittance increases with frequency, while the equivalent capacitance associated with their imaginary part strongly depends on frequency. As explained in [45, 58], values of α_i coefficients lower than 1 are the signature of dispersive and distributed behavior induced by disorder and inhomogeneities in the material. These values induce admittance real(Z_{CPE}) not equal to zero and a frequency-dependent capacitance associated with the imaginary part of Z_{CPEi}. The frequency-dependent admittance contribution adds to resistance R_2 or R_3 in order to fully model the transport in Fe_3O_4 and GNP. The similar behavior is even more pronounced in sample 40 wt%, but not shown here for the sake of brevity. Q8

3.4. Comparison of models

In this paper, we introduced three different models. Table 1 reveals that the thermionic model presented in section 3.1 is not able to clearly discriminate between the three samples, since extracted values from the fitting of equation (1) are very close. We explain this by the fact that model (1) does not represent properly the transport in disorder nanomaterials as represented schematically in figure 3(b). Therefore, we proposed to investigate in section 3.2.2 the DRRN model. Table 2 reveals that better discrimination between samples is obtained. The DRRN conductance model results from homogeneization over various conductances associated with different percolative channels through the Fe_3O_4@GNP composite, revealing that distributed mechanisms are involved in the transport. This is in line with the 'random' hypothesis of the model so that increasing the concentration in Fe_3O_4 NPs induces more disorder in the system. Next, the impedance spectroscopy model developed in section 3.3.2 reveals that a CPE is necessary to obtain an accurate fit of the measured Cole–Cole response to the response of the equivalent circuit, which confirms that disorder of transport occurs in the AC regime. Tables 3 and 4 show that for samples 28 wt% and 40 wt% the coefficients α_1 and α_2 deviate from unity. This is reported to be related to distributed circuits associated with disorder in the material, this time clearly evidenced in the AC regime through the presence of CPE elements. Also, the comparison of tables 1–4 reveals that DC flow is less sensitive than AC flow in terms of concentration and bias, which means the frequency-dependent AC properties are more sensitive to the morphology of the nanocomposite than DC properties.

The bias-dependent equivalent *RLC*-circuit is useful for the design of tunable devices for communication and RF applications [61, 62], namely metamaterials using varying surface impedance in frequency-selective surface structures. The present study focuses on iron oxide, but oxides of other transition metal elements such as yttrium and manganese could be the subject of future works based on similar considerations.

4. Conclusion

This paper analyzed the DC and AC electrical responses of magnetically functionalized GNPs having different LRs of Fe_3O_4 NPs. Three different models were proposed to assess the nonlinearity of electronic transport. The thermionic model does not provide good discrimination between the samples as a function of iron oxide amount. The DRRN model, assuming a spatial distribution of resistances, allows better discrimination, since GNPs having high loadings of magnetite (40 wt% and 28 wt%) show nonlinear current behavior while the 17 wt% loaded sample possesses more linear ohmic characteristics. The hypothesis of distribution is confirmed through an equivalent-circuit model: the presence of CPE provides a good fitting of Cole–Cole plots of impedance and is associated with the distributed electronic disorderness in the samples. Due to the nonlinearity observed in these samples, a tunable impedance effect is obtained in the range 10–100 MHz at different applied DC biases, with capacitive behavior due to the high loading of Fe_3O_4 NPs that act as dielectric spacers between graphitic nanosheets.

Acknowlegments

The authors are grateful to the National Fund for Scientific Research (F.R.S.-FNRS, Belgium) for supporting this research. This work is also supported by the Walloon region, and by the 'Communauté Française de Belgique', through the project 'Nano4waves' funded by its research program 'Actions de Recherche Concertées'. Special thanks are also due to Profs A Delcorte and C Bailly for fruitful discussions in the frame of the Nano4waves project, and to Mr P Simon for his help with the measurements.

ORCID iDs

Sophie Hermans https://orcid.org/0000-0003-4715-7964
Isabelle Huynen https://orcid.org/0000-0002-8504-2896

References

[1] Mederos-Henry F, Pichon B P, Yagang Y T, Delcorte A, Bailly C, Huynen I and Hermans S 2015 *J. Mater. Chem* C **4** 3290–303
[2] Mederos-Henry F, Mahin J, Pichon B P, Dîrtu M M, Garcia Y, Delcorte A, Bailly C, Huynen I and Hermans S 2019 *Nanomaterials* **9** 1196
[3] Kazi S N, Badarudin A, Zubir M N M, Ming H N, Misran M, Sadeghinezhad E, Mehrali M and Syuhada N I 2015 *Nanoscale. Res. Lett.* **10** 212
[4] Lu J, Guan X-T, Fan L-Z, Cao W-Q, Zhao Q-L, Wang C-Y and Cao M-S 2015 *Mater. Res. Bull.* **72** 316–23
[5] Song W L, Guan X-T, Fan L-Z, Cao W-Q, Zhao Q-L, Wang C-Y and Cao M-S 2015 *Mater. Res. Bull.* **72** 316–23
[6] Lee J H, Shin W H, Ryou M-H, Jin J K, Kim J and Choi J W 2012 *Chem Sus Chem* **5** 2328–33 201
[7] Vicarelli L, Vitiello M S, Coquillat D, Lombardo A, Ferrari A C, Knap W, Polini M, Pellegrini V and Tredicucci A 2012 *Nat. Mater.* **11** 865–71
[8] He Q, Wu S, Yin Z and Zhang H 2012 *Chem. Sci.* **3** 1764–72
[9] Liang J, Xu Y, Sui D, Zhang L, Huang Y, Ma Y, Li F and Chen Y 2010 *J. Phys. Chem.* C **114** 17465–71
[10] Miao X, Tongay S, Petterson M K, Berke K, Rinzler A G, Appleton B R and Hebard A F 2012 *Nano Lett.* **12** 2745–50
[11] Miao X *et al* 2016 *Advances in Carbon Nanostructures* eds Silva Adrian M T and Carabineiro Sonia A C (InTech)
[12] Rodrıguez-Manzo J A, Cretu O and Banhart F 2010 *ACS Nano* **4** 3422–8
[13] Huang X *et al* 2011 *Small* **7** 1876
[14] Rebuttini V 2014 Functional iron oxide-based hybrid nanostructures PhD Thesis
[15] Zhan Y, Meng F, Yang X, Zhao R and Liu X 2011 *Mater. Sci. Eng.* B **176** 1333–9
[16] Li , Li L, Qin R, Li H, Yu L, Liu Q, Luo G, Gao Z and Lu J 2011 *ACS Nano* **5** 2601–10
[17] Tung T, Feller J-F, Kim T, Kim H, Yang W S and Suh K S 2012 *J. Polym. Sci.* **50** 927–35
[18] Chen Y, He J, Li G, Tang J, Wang T, Guo Y and Xue H 2013 *J. Mater. Chem.* C **1** 765–77
[19] Yang S, Feng X, Ivanovici S and Müllen K 2010 *Chem. Int. Ed.* **49** 8408–11
[20] Wu W *et al* 2008 *Nanoscale Res. Lett.* **3** 397–415
[21] Cava C E, Persson C, Zarbin A J G and Roman L S 2014 *Nanoscale* **6** 378
[22] Fan Z W, Li P, Zhang L T, Mi W B, Jiang E Y and Bai H L 2012 *Thin Solid Films* **520** 3641
[23] Feng X 2015 *Nanocarbons for Advanced Energy Storage* vol 1 (Wiley-VCH Verlag GmbH & Co)
[24] Peik-See T, Pandikumar A, Nay-Ming H, Hong-Ngee L and Sulaiman Y 2014 *Sensors* **14** 15227–43
[25] Sangiovanni D G, Gueorguiev G K and Kakanakova-Georgieva A 2018 *Phys. Chem. Chem. Phys.* **20** 17751
[26] Li S S *et al* 2014 *RSC Adv.* **4** 7500
[27] Bacaksizet C, Sahin H, Ozaydin H D, Horzum S, Senger R T and Peeters F M 2015 *Phys. Rev.* B **91** 085430
[28] Dos Santos R B *et al* 2016 *Nanotechnology* **27** 14560
[29] Eul H and Schiek B 1991 *IEEE Trans. Instr. Meas.* **40** 732–5
[30] Oueriemi I, Raskin J-P, Choubani F and Huynen I 2013 *Microwave Opt. Technol. Lett.* **55** 2648–52
[31] Gevorgian S S *et al* 1996 *IEEE Trans. Microwave Theory Tech.* **44** 896–904
[32] Yagati A K *et al* 2016 *Sensors* **16** 109
[33] Pampin R *et al* 2020 *J. Electroanal. Chem.* **856** 113651
[34] Lee S, Fursina A, Mayo J T, Yavuz C T, Colvin V L, Sumesh Sofin R G, Shvets I V and Natelson D 2007 *Nat. Mater.* **7** 130–3
[35] Fursina A 2010 Investigation of electrically driven transition in magnetite, Fe_3O_4 nanostructures PhD Thesis
[36] Klinqer M I and Samoehvalo A A 1977 *Phys. Stat. Sol.* B **79** 9–48
[37] Jordan K *et al* 2006 *Phys. Rev.* B **74** 085416
[38] Zhou J *et al* 2011 *RSC Adv.* **1** 782–91
[39] Watts S M *et al* 2005 *Appl. Phys. Lett.* **86** 212108
[40] Chakrabarty R K, Bardhan K K and Basu A 1991 *Phys. Rev.* B **44** 6773–9
[41] Gefen Y and Shih W E 1986 *Phys. Rev. Lett.* **57** 3097–100
[42] Gupta A K and Sen A K 1998 *Phys. Rev.* B **57** 3375
[43] He L X and Tjong S C 2010 *Synth. Met.* **160** 2085–8
[44] Hu G and Suzuki Y 2002 *Phys. Rev. Lett.* **89** 276601
[45] Zeng H, Black C T, Sandstrom R L, Rice P M, Murray C B and Sun S 2006 *Phys. Rev.* B **73** 020402(R)
[46] Shoar Abouzari M R, Berkemeier F, Schmitz G and Wilmer D 2000 *Solid State Ion.* **180** 922–7
[47] Tang Y 2013 *IEEE Trans. Microwave Theory Tech.* **61** 1870–8
[48] Dobrowolski J 2010 *Microwave Network Design Using the Scattering Matrix* (Artech House)

[49] Suman C K, Yun J, Kim S, Lee S-D and Lee C 2009 *Curr. Appl. Phys.* **9** 978–84
[50] Varade V *et al* 2013 *J. Phys. D: Appl. Phys.* **46** 365306
[51] Laibowitz R B 1984 *Phys. Rev. Lett.* **53** 380–3
[52] Pozar D 1994 *Mjcrowave Engineering* 4th edn (New York: Wiley)
[53] Barsoukov E and Macdonald J R (eds) 2005 *Impedance Spectroscopy: Theory, Experiment, and Applications* 2nd edn (New York: Wiley)
[54] Hischornn , Hirschorn B, Orazem M E, Tribollet B, Vivier V, Frateur I and Musiani M 2010 *J. Electrochem. Soc.* **157** C452–7
[55] Chen C C, Huang B-C, Lin M-S, Lu Y-J, Cho T-Y, Chang C-H, Tien K-C, Liu S-H, Ke T-H and Wu C-C 2010 *Org. Electron.* **11** 1901–8
[56] Hirschorna B, Orazem M E, Tribollet B, Vivier V, Frateur I and Musiani M 2010 *Electrochim. Acta* **55** 6218–27
[57] Hirschorn B, Orazem M E, Tribollet B, Vivier V, Frateur I and Musiani M 2010 *J. Electrochem. Soc.* **157** C458–63
[58] Hirschorn B *et al* 2010 *J. Electrochem. Soc.* **157** C452–7
[59] Jeppe C and Dyre J 1988 *Appl. Phys.* **64** 2456
[60] Tjong S C 2012 *Polymer Composites with Carbonaceous Nanofillers: Properties and Applications* (Wiley-VCH Verlag & Co)
[61] Gholipur R and Bahari A 2016 *Mater. Chem. Phys.* **180** 135–43
[62] Gholipur R and Bahari A 2015 *Opt. Mater.* **50** 175–83

Q11